



## How monomer concentrations influence structures and separation performances of polyamide nanofiltration membranes?

Gan Liu<sup>a</sup>, Mingjie Wei<sup>a,\*</sup> , Zhaoqin Xu<sup>b</sup> , Daiwen Li<sup>a</sup>, Ming Liu<sup>a</sup>, Jun Huang<sup>a</sup>, Zhe Zhang<sup>b</sup>, Yong Wang<sup>a,c</sup>

<sup>a</sup> State Key Laboratory of Materials-Oriented Chemical Engineering, College of Chemical Engineering, Nanjing Tech University, Nanjing, 211816, Jiangsu, China

<sup>b</sup> School of Environmental Science and Engineering, Nanjing Tech University, Nanjing, 211816, Jiangsu, China

<sup>c</sup> School of Energy and Environment, Southeast University, Nanjing, 210096, Jiangsu, China

### ARTICLE INFO

#### Keywords:

Polyamide  
Nanofiltration  
Interfacial polymerization  
Water traces

### ABSTRACT

Understanding the microscopic architecture as well as the formation mechanisms of polyamide separation layer is essential for designing nanofiltration (NF) membranes with better performance. The influence of monomer concentrations on the structure and separation performance of polyamide NF membranes are investigated using molecular dynamics simulations. By simulating the interfacial polymerization reaction between piperazine (PIP) and trimesoyl chloride (TMC) in a dual-solvent environment, four NF membranes are constructed using four different monomer ratios. Nonequilibrium molecular dynamics simulations are then employed to evaluate water permeance and ion rejection properties of the resulting membranes. Results show that monomer concentrations control critical membrane structural features like thickness and degree of network cross-linking (DNC) by tuning diffusion-reaction kinetics in interfacial polymerization, consequently altering water and ion transport pathways. Lower PIP concentrations promote decreased DNC and membrane density, enhancing water flux via the permeation paths. Molecular transport pathways and the dehydration behavior of ions reveal the synergistic effects of pore morphology and hydration shell modulation on membrane selectivity. These findings provide theoretical guidance for optimizing fabrication conditions and enhancing the separation performance of polyamide NF membranes.

### 1. Introduction

Water scarcity has emerged as a pressing global challenge nowadays. In addressing this issue, membrane-based technologies for seawater desalination and water reuse have emerged as among the most promising solutions. Despite the considerable research efforts aimed at enhancing the water permeability of desalination membranes [1], recent studies have demonstrated that further permeability enhancements result in only marginal improvements in energy efficiency [2]. Consequently, there has been a shift in research focus toward the development of membranes with ultrahigh water-solute selectivity, to achieve a balance between energy efficiency and separation performance.

Among the existing membrane technologies, nanofiltration (NF) membranes have been widely used for rejecting divalent cations and small organic molecules owing to their low operating pressure and high separation efficiency [3–5]. Most advanced NF membranes are typically fabricated with a thin-film composite (TFC) structure, comprising a

dense selective layer supported by a porous substrate. Although the porous substrate can influence membrane performance by regulating the formation of the polyamide selective layer [6–11] and controlling the transport pathways of water and solutes [12–15], the key factor directly determining the separation performance of NF membranes remains the polyamide selective layer itself. The thickness, degree of network cross-linking (DNC) and pore size distribution of this layer are critical in controlling membrane permeability and selectivity [16].

The polyamide selective layer is generally synthesized via interfacial polymerization (IP), in which amine monomers diffuse from the aqueous phase into the organic phase and react with acyl chloride monomers in the interfacial region, to form a polyamide membrane with a sub-nanometer pore structure. In order to achieve both high permeability and high selectivity, the selective layer of TFC membranes is expected to be ultrathin and highly cross-linked [17–19]. The intrinsic properties of the selective layer, including surface charge, surface morphology, hydrophilicity, chemical functionality, and pore size, significantly

\* Corresponding author.

E-mail address: [mj.wei@njtech.edu.cn](mailto:mj.wei@njtech.edu.cn) (M. Wei).

<https://doi.org/10.1016/j.memsci.2025.124334>

Received 29 April 2025; Received in revised form 9 June 2025; Accepted 12 June 2025

Available online 13 June 2025

0376-7388/© 2025 Elsevier B.V. All rights reserved, including those for text and data mining, AI training, and similar technologies.

influence membrane separation performance by determining the interactions between water and solutes within the membrane [20–23]. Consequently, the optimization of the structure and properties of the selective layer is imperative for enhancing membrane performance.

To achieve these goals, researchers have conducted extensive studies on IP conditions. By adjusting monomer type and concentration, reaction time, and curing conditions, interfacial reaction processes can be optimized to enhance membrane structure and performance [19,24,25]. Further investigations have delved into the diffusion and formation mechanisms of the polyamide layer during IP. For instance, Zhang et al. [26] managed to control the diffusion rate by freezing the aqueous phase, enabling an in-depth analysis of the effects on membrane morphology and performance. Karan et al. [27] regulated the interfacial reaction rate by controlling diamine release at the water-hexane interface, successfully fabricating a morphology-controlled polyamide nanofilms on a nanostrand layer.

When studying the transport mechanisms of polyamide membranes, commonly used models such as the Pore Flow (PF) model, the Solution Diffusion (SD) model [28,29]. Moreover, the Donnan-Steric Pore Model with Dielectric Exclusion (DSPM-DE) model [30] simplify membrane pores by treating them as homogeneous, rigid, and parallel cylindrical channels. However, the selective layer of polyamide NF membranes possesses a highly complex and flexible internal structure, where ion transport pathways are often tortuous and intricate. While the DSPM-DE model has been demonstrated to be effective in predicting ion partitioning and permeation through its ability to effectively fit experimental data, it still lacks the capacity to capture the structural intricacies of the membrane. Since the transmembrane transport mechanism of ions is closely related to the actual morphology of membrane pores, a comprehensive analysis of the distribution and configuration of membrane pores is essential for accurately elucidating transport mechanisms and providing insights into optimizing membrane selectivity and permeability.

Recent experimental efforts have proposed several methods for fabricating high-permeability seawater desalination membranes by controlling the internal structure, surface morphology, thickness, and other characteristics of the polyamide selective layer [27,31–33]. However, the precise correlation between nanoscale polyamide morphology and membrane performance remains unclear [34]. As a powerful supplement to the experimental research, molecular dynamics (MD) simulations serve as a powerful tool for investigating the transport of small molecules through nanopores, enabling the exploration of transport characteristics that are difficult to capture experimentally. However, most MD studies have primarily focused on monomer diffusion or the characterization of bulk membrane properties [35–38]. In contrast, systematic investigations into the membrane formation process and the resulting internal microstructure remain limited [39].

To address this issue, we constructed NF membrane models by simulating the IP reaction between piperazine (PIP) and trimesoyl chloride (TMC) monomers in a dual-solvent environment. Specifically, we allowed an aqueous phase containing PIP and water molecules to contact an oil phase containing TMC and n-hexane, where PIP monomers freely diffused to the interface driven by the concentration gradient and reacted with TMC to form the polyamide membrane structure by IP reaction. Then, we used non-equilibrium molecular dynamics (NEMD) simulations to evaluate the water permeance and solute rejection performance of the obtained membranes. By analyzing the transport pathways of water molecules and ions within the membrane, we identified the main characteristics of the transport process and their relationship with the membrane structure, providing a theoretical basis for further membrane performance optimization.

## 2. Simulation methods

### 2.1. Construction of polyamide membranes in a dual-solvent environment

The initial molecular structures of PIP and TMC were constructed using the moltemplate software [40], ensuring that all monomer molecules remained intact in their original structures [41,42]. In most experimental studies, the concentration of PIP and TMC varies over a relatively wide range [24,43]. Considering the limitations of system size and computational efficiency, the PIP concentration in the simulation was restricted to below 2.00 wt%. For the organic phase solvent, n-hexane was selected. Due to its low density, using a low concentration would require a significantly larger simulation system, which would severely impact computational efficiency. Therefore, its concentration had to be increased accordingly. The concentration of TMC was determined based on the specific molar ratios listed in Table 1. The case names in the following discussion are abbreviated according to the four cases listed.

Based on the concentration parameters listed in Table 1, we constructed a biphasic system consisting of an aqueous solution of PIP and a hexane solution of TMC, where the reactive monomers were randomly distributed in the two phases. Subsequently, graphene sheets were introduced at both ends of the system as constraint boundaries, and a pressure of 1 bar was applied. Then a 1 ns simulation was performed in a canonical ensemble (NVT) ensemble at a constant temperature of 300 K to ensure sufficient equilibrium. The dimensions of the simulation box were set to  $L_x = L_y = 5.1$  nm, while the z-direction size was dynamically adjusted according to the reaction progress. Its value was kept significantly larger than the gap between the two graphene sheets to minimize intermolecular interactions across periodic boundaries. Except the fixed graphene sheets, all molecules in the system were allowed to move freely. The constructed model is shown in Fig. 1(a).

The cross-linking reaction followed the principle of spontaneity and was implemented using a self-developed program called the interfacial polymerization simulator (IPS) [44]. This program continuously tracked the distance between the carbon atoms of the acyl chloride groups in the TMC molecules and the nitrogen atoms of the amine groups in the PIP molecules. When the distance fell below a predefined threshold of 0.35 nm, a new amide bond was formed [45,46]. The reaction tracking interval was set to 0.05 ns. To maintain the stability of the reaction system concentration, the solution concentration was simultaneously tracked during each cross-linking detection step. Monomers were dynamically replenished as needed to ensure that the concentrations of TMC and PIP remained their initial values.

### 2.2. Post-treatment process

In this study, membrane structure optimization was achieved through a self-designed post-treatment process. After the cross-linking reaction, the following steps were sequentially performed: (1) Removal of residual solvents and unreacted monomers and retain only the main body of the membrane structure: As shown in Fig. 1(b), the green boxed region represents the retained portion. (2) Curing simulation: The system temperature was raised to 350 K to simulate the experimental curing process. Due to the accelerated reaction rate at this stage, the reaction tracking interval was shortened to 0.01 ns. (3)

**Table 1**  
Concentrations and numbers of monomers in each simulation case.

Case Name	Concentration (wt.%)		Monomer Number	
	PIP	TMC	PIP	TMC
M12/2	2.00	1.54	12	2
M6/2	1.00	1.54	6	2
M3/2	0.50	1.54	3	2
M3/8	0.50	6.18	3	8

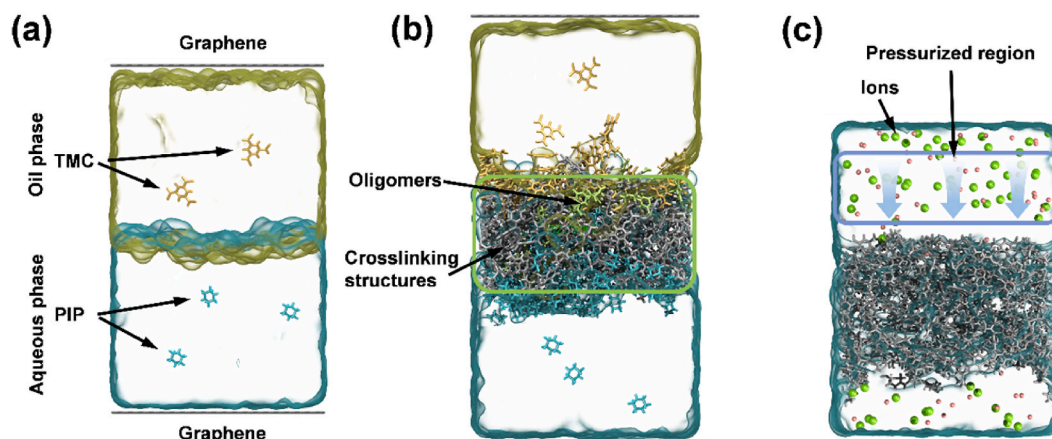


**Fig. 1.** Schematic of the simulation process. (a) Initial configuration for IP; (b) Final state after cross-linking, with the main membrane region highlighted in the green box, which is retained for curing; (c) Model used for evaluating water permeation and solute rejection.

Elimination of low molecular weight oligomers: Oligomers with less than 200 atoms were removed by molecular weight screening to avoid structural defects caused by high-pressure water flow in subsequent NEMD simulations. (4) Hydrolysis of residual acyl chloride groups: Residual acyl chloride groups were hydrolyzed to form carboxyl groups to improve the chemical stability of the polyamide membranes.

The dry polyamide membrane obtained after the above treatment required additional hydration process to meet the requirements for permeability testing. First, we utilized the molecule insertion function within the IPS software to insert as many water molecules as possible into the polyamide membrane structure until no more space was readily available to accommodate additional water molecules. A pressure of 1 bar was then applied across the graphene layers, followed by a 10-ns equilibrium molecular dynamics (EMD) simulation. The EMD simulation continued until the distribution of water molecules in each polyamide membrane reached dynamic equilibrium and the system energy fluctuations stabilized, providing a reliable initial configuration for subsequent non-equilibrium permeation simulations.

### 2.3. NEMD simulation process

The transmembrane transport behavior was then investigated using the NEMD simulations [47]. The NEMD simulation system was constructed as follows: a given number of ions were randomly distributed in the aqueous phase on both sides of the membrane, forming a saline solution of  $1 \text{ mol L}^{-1}$  for either  $\text{Na}^+$  or  $\text{Mg}^{2+}$ . A directional pressurized field was applied to water molecules within a 1 nm wide region at a certain distance from the membrane surface. The pressurized field intensity was determined by the equation  $f = \Delta P A / n$ , where  $\Delta P$  is the predefined transmembrane pressure drop, set to 300 MPa,  $A$  is the cross-sectional area of the simulation box, and  $n$  is the total number of water molecules within the pressurized region.

It is worth noting that a relatively high pressure drop was chosen to improve the signal-to-noise ratio, a common strategy to obtain meaningful data within the limited simulation time. The constructed model is shown in Fig. 1(c), where the blue box indicates the pressure application region. To prevent significant membrane displacement under high pressure, elastic potential constraints were applied to the top and bottom layers of the membrane, with a force constant set to 0.2, ensuring that the membrane retained adequate mobility. The system temperature was maintained at 300 K, with temperature calculations adjusted by subtracting the center-of-mass velocity of the water molecules.

The NEMD simulations were run for a total of 100 ns with a time step of 1 fs. The first 50 ns were used for reaching steady state, while the remaining 50 ns were used for further analysis. A comprehensive analysis of various membrane parameters and performance metrics can be

found in the supplementary materials.

### 2.4. Additional simulation details

The entire simulation process was implemented using IPS coupled with LAMMPS [48]. Molecular modeling was performed following a multi-scale parameterization strategy: organic molecules (hexane, TMC, and MPD) were parameterized based on the GAFF2 force field [49], with atomic charges determined using density functional theory (B3LYP/6-311G\*\*) combined with the RESP fitting method. Water molecules were modeled using the standard SPC/E model [50], and the SHAKE algorithm was used to constrain the water geometry and improve computational efficiency.

Non-bonded interactions were treated using the Lorentz-Berthelot mixing rules, with a Lennard-Jones (LJ) potential cutoff radius of 1.5 nm. Long range electrostatic interactions were calculated using the PPPM method for accuracy. To minimize disturbances from the graphene-bounded boundaries at the reactive interface, the LJ potential parameters of graphene were modified, with  $\epsilon$  reduced to 1 % of its baseline value, and a short-range cutoff of 1.0 nm.

The simulations were performed under three-dimensional periodic boundary conditions (PBC). The equations of motion were integrated using the leap-frog algorithm with a 1 fs time step. The system temperature and pressure were controlled using a Nose-Hoover thermostat and barostat, respectively. The NVT ensemble was used for key reaction steps [51].

## 3. Results and discussion

### 3.1. Membrane performance

The pursuit of excellent membrane performance is a common goal among researchers. Therefore, we first present the water permeance and ion rejection results for various NF membranes obtained using the IPS. As shown in Fig. 2, the water permeance of the membranes in this study ranges from 103.2 to 390.5  $\text{L m}^{-2} \text{ h}^{-1} \text{ bar}^{-1}$  (LMHB), with  $\text{Na}^+$  rejection varying from 2.8 % to 65.5 %. To account for the influence of membrane thickness and facilitate a more intrinsic comparison of material transport properties, the water permeability (LMH-nm/bar) was also calculated and is presented in the supplementary materials. However,  $\text{Na}^+$  rejection alone is not sufficient to fully evaluate the ion rejection performance of the NF membranes. Therefore, we further tested divalent cations, using  $\text{Mg}^{2+}$  as a representative. The results show that  $\text{Mg}^{2+}$  rejection ranges from 53.3 % to 94.2 %, indicating that these NF membranes exhibit effective separation for both monovalent and divalent cations.

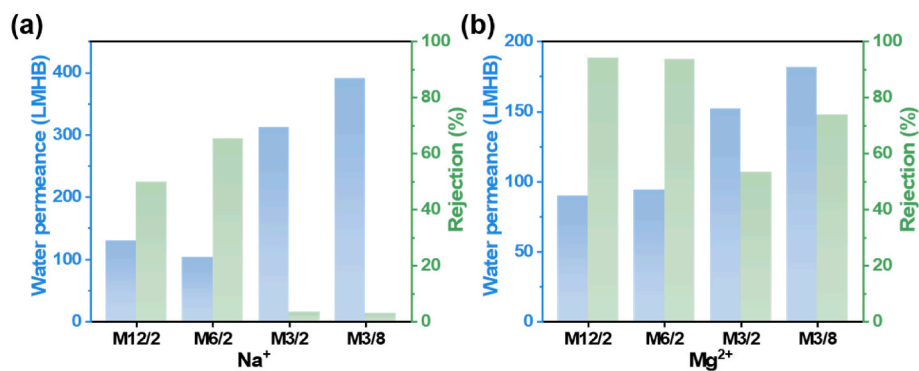


Fig. 2. Permeance and ion rejection performance of all membranes: (a) Performance of NaCl solution and (b) that of MgCl<sub>2</sub> solution.

Based on the rejection results of two types of cations, the selectivity of Na<sup>+</sup>/Mg<sup>2+</sup> can be calculated for each case as,

$$S_{Na/Mg} = \frac{1 - R_{Na}}{1 - R_{Mg}} \quad (1)$$

where  $R_{Na}$  and  $R_{Mg}$  are the rejection results for Na<sup>+</sup> and Mg<sup>2+</sup>, respectively.  $S_{Na/Mg}$  results for M12/2 and M6/2 are 8.64 and 5.48, respectively, which are obviously higher than those for M3/2 ( $S_{Na/Mg} = 2.07$ ); M3/8 ( $S_{Na/Mg} = 3.72$ ). However, water permeance of M12/2 and M6/2 is as low as around 100 LMHB while that of M3/2 and M3/8 is at least twice, indicating that these four NF membranes obey the trade-off effect.

The performance of these four NF membranes is related to the variations of their internal microstructure. It is necessary to further study the microstructure of these NF membranes. The primary factors affecting the permeability and rejection performance of NF membranes are their microstructure, with membrane thickness being particularly critical.

The water permeance values presented in Fig. 2 are significantly higher than typical experimental values reported in the literature for polyamide nanofiltration membranes, which are approximately 10–30 LMHB [52]. This discrepancy is due to the limited system size in the simulations. The polyamide NF membranes constructed in this work have an average thickness of 3.1, 5.1, 3.3 and 3.0 nm for M12/2, M6/2, M3/2 and M3/8, respectively, which is far below those of the experimental membranes. The reason is that the presence of a free interface significantly reduces the thickness of the fabricated membrane, and a thinner membrane results in a nonlinear and large increase in water

permeability that far exceeds the change in thickness [53]. When water molecules or ions pass through the membrane, they tend to follow the path of least resistance [54]. Therefore, permeation occurs predominantly in the thinner, more porous regions of the membrane rather than in the thicker, denser regions. At this point, it is unreliable to examine the contribution of the average thickness to permeance when considering the NF membrane as a whole. By using MD simulations, which provide a detailed view of the microstructure, we are able to present more comprehensive results related to membrane thickness.

As shown in Fig. 3(a), all four NF membranes are nearly defect free and structurally intact before permeance examination. However, after undergoing NEMD simulations with water flow impact, the microstructure of membranes changes to varying degrees for four NF membranes (Fig. 3(b)). For M12/2 and M6/2 membranes, the thickness distribution slightly changes. Regions exhibiting noticeably low thickness are observed. The changes in thickness distribution certainly influence the performance of these NF membranes. The M6/2 membrane is generally thicker and exhibits a uniform thickness distribution. Even after enduring water flow impact in the NEMD simulations, it maintains its structural integrity, thereby ensuring complete rejection of Mg<sup>2+</sup> and high rejection of Na<sup>+</sup>. In contrast, the M12/2 membrane develops small low-thickness regions after water flow impact, which provide pathways for water molecules and some Na<sup>+</sup> to penetrate. Consequently, its Na<sup>+</sup> rejection rate is slightly lower than that of the M6/2 membrane while its permeance is somewhat higher. For the M3/2 and M3/8 membranes, larger low-thickness regions are observed in the thickness maps, which significantly reduce the permeation resistance for both ions and water

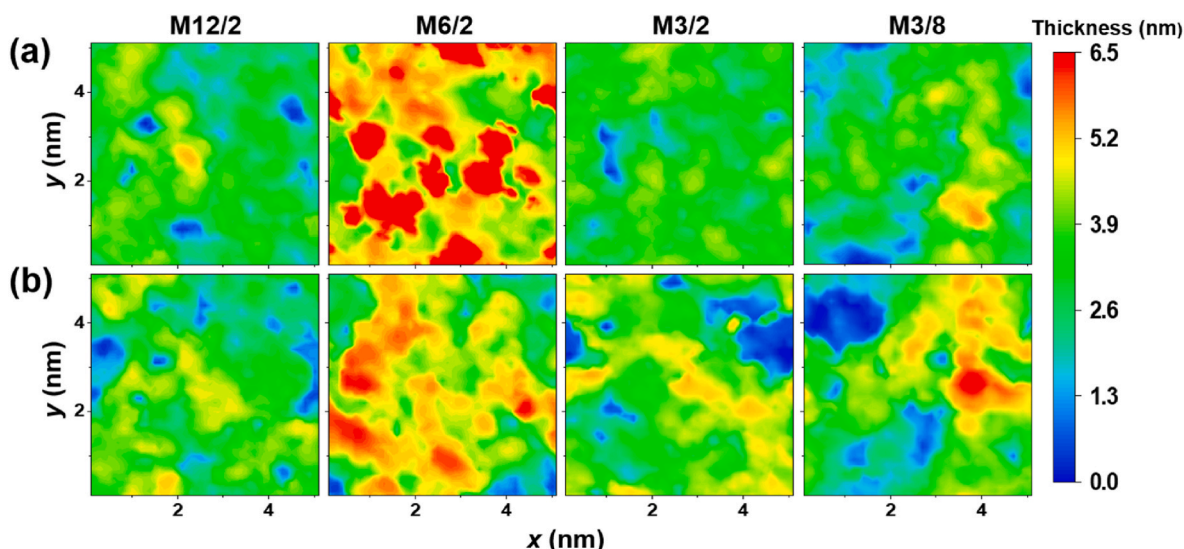


Fig. 3. xy-plane thickness maps of all membranes before (a) and after (b) NEMD simulations.

molecules, leading to lower rejection rates for both cations and higher water permeance.

### 3.2. Molecular details during the formation of NF membranes

The differences among the four NF membranes are correlated with their fabrication conditions. Therefore, understanding the relationship between membrane structure and various factors in the fabrication process is highly essential in this work.

Firstly, the variations in membrane thickness are examined. Given the high reaction constant of PIP, its reaction with TMC is often approximated as instantaneous; under such conditions, membrane thickness is generally considered to be primarily governed by monomer diffusion behavior during the IP process [44]. To gain deeper insights into the complex influence of monomer concentration on thickness, we examined existing theoretical models of interfacial polymerization. For instance, the mathematical model proposed by Freger and Srebnik [55] explored the relationship between membrane thickness and monomer concentration, predicting a decrease in thickness with increasing concentration based on its specific assumptions. While this macroscopic theoretical model provides a framework for understanding general trends regarding the effect of monomer concentration on membrane growth, it often simplifies the intricate diffusion-reaction kinetics at the interface. Specifically, it offers limited direct insight into the precise micromechanisms by which varying monomer stoichiometric ratios regulate the local reaction environment, oligomer behavior, and ultimately, the final membrane microstructure.

Under the premise of maintaining consistent initial monomer concentrations, our molecular dynamics simulations revealed a more complex dependence of membrane thickness on the monomer ratio, highlighting the critical importance of local stoichiometric balance and kinetic competition. When the aqueous phase PIP concentration is excessively high, the monomer ratio at the interface becomes imbalanced, leading to a tendency for PIP to diffuse excessively into deeper regions of the organic phase. However, due to the relative scarcity of TMC in these deeper regions, these over-diffused PIP molecules struggle to react effectively and are instead attracted back towards the interface by locally accumulated TMC, resulting in a narrower effective reaction zone and a decrease in membrane thickness.

Conversely, when the PIP concentration is moderately reduced, fostering a more balanced PIP-to-TMC ratio at the interface, the total amount of PIP entering the organic phase may decrease, but the probability and depth of its effective film-forming reaction with TMC are optimized. At this stage, the resulting low-mobility oligomers are less prone to diffusing back towards the interface and can react further with TMC within the organic phase, thereby promoting an increase in membrane thickness. However, if the PIP concentration is excessively low, the relative excess of TMC at the interface can lead to the rapid formation of a dense layer at the immediate interface, significantly inhibiting effective PIP penetration and diffusion into the organic phase. This also confines the reaction zone to an extremely thin interfacial layer, ultimately resulting in a thinner membrane.

Moreover, it is noteworthy that higher overall monomer concentrations also lead to an accelerated reaction process (Fig. S4), which can further contribute to limiting membrane growth. This observation aligns with the conclusions of the Freger-Srebnik model, which predicts a decrease in membrane thickness with increasing monomer concentration. Therefore, we posit that the molar ratio of the two monomers and their local effective concentrations within the interfacial region, rather than merely their initial bulk concentrations, collectively dictate the depth of the interfacial polymerization reaction zone and, consequently, the final membrane thickness.

Since polyamide membrane fabrication fundamentally involves the cross-linking process, which determines the membrane structure, the degree of network cross-linking (DNC) is calculated for each membrane by Equation (2) [27,56]:

$$\text{DNC} = \frac{X}{X + Y} \times 100\% \quad (2)$$

The calculation method is based on the two structural forms produced by the reaction between TMC and amine monomers: the number of fully cross-linked structures ( $X$ ), where all acid chloride groups ( $\text{Cl}-\text{C}=\text{O}$ ) of TMC react with amine monomers to form amide bonds, and the number of fully linear structures ( $Y$ ), where one acid chloride group of TMC remains unreacted.

As shown in Fig. 4(a), after the completion of the IP process, the DNC of the membranes follows the trend:  $\text{M12/2} > \text{M6/2} > \text{M3/2} > \text{M3/8}$ . The reason for this trend is that a relatively higher PIP concentration provided more reactive sites for TMC, thereby increasing the DNC. However, in the case of M3/8, excessive TMC results in a lower DNC.

In the experimental preparation of NF membranes, post-treatment is required after IP to further increase DNC and improve membrane integrity. In this work, we simulated the post-treatment process and calculated the changes in DNC after post-treatment. As shown in Fig. 4(a), the DNC of all membranes increases after post-treatment, with M6/2 and M3/2 exhibiting the most significant improvement. However, for M12/2 and M3/8, the increase in DNC is relatively limited. This is primarily due to the fact that, during the IP process, the higher concentration of one kind of monomer results in the almost complete consumption of the other kind of monomer (Fig. S1), thereby limiting the number of functional groups available for further reaction during post-treatment, and consequently restricting the enhancement of cross-linking.

Moreover, after post-treatment, the DNC and thickness distribution (Fig. 3(a)) of the M12/2 membrane become similar to those of M3/2. However, as shown in Fig. 1, its permeance is significantly lower than that of M3/2, and no noticeable defects are observed after the NEMD simulation (Fig. 3(b)), indicating that its structure is denser and more intact. As shown in Fig. 4(b), the local maximum density of M12/2 is higher than that of M3/2, further confirming its denser membrane structure, which enables it to confront the impact of higher-pressure water flow. For the M6/2 membrane, its local maximum density is close to that of M12/2, and its overall thickness represented by the density distribution width in Fig. 4(b) is also greater. Therefore, under high-pressure water flow, it exhibits no significant structural damage. At this time, its permeance is greatly limited because of the highest transport resistance.

### 3.3. Traces of permeated water molecules

Generally, the variations in membrane thickness play a key role in water permeance. As discussed above, the membrane heterogeneity also critically influences permeation behavior. To identify the dominant factors governing water transport, the trajectories of water molecules across the membranes are analyzed singly. Since there exist water clusters confined within the membranes, which did not permeate across the membranes during the NEMD simulations, only water molecules that successfully crossed the membrane are selected to clarify their transport mechanisms.

Firstly, the overall distribution of water molecules permeating through the membrane is plotted while noise data with excessively low local density values are removed (method in the supplementary materials) to accurately reflect the primary distribution regions of water molecules. As shown in Fig. 5(a), the distribution characteristics of water molecules vary significantly among different membrane cases. From the three-dimensional distribution plots and their density projections onto the  $xy$ -plane (hereafter referred to as the water molecule distribution regions), it is evident that water molecules primarily accumulate in several distinct transmembrane regions.

Specifically, in the M3/2 and M3/8 membranes, the distribution of water molecules is relatively straight and concentrated, with distinct high-density regions. This indicates that most of the water molecules

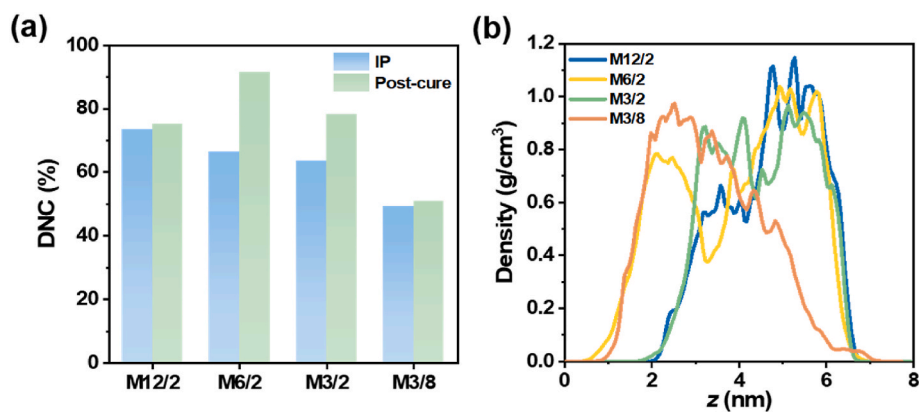


Fig. 4. DNC (a) and density distribution along  $z$  direction (normal to the membrane surface) of membranes after post-cure process (b).

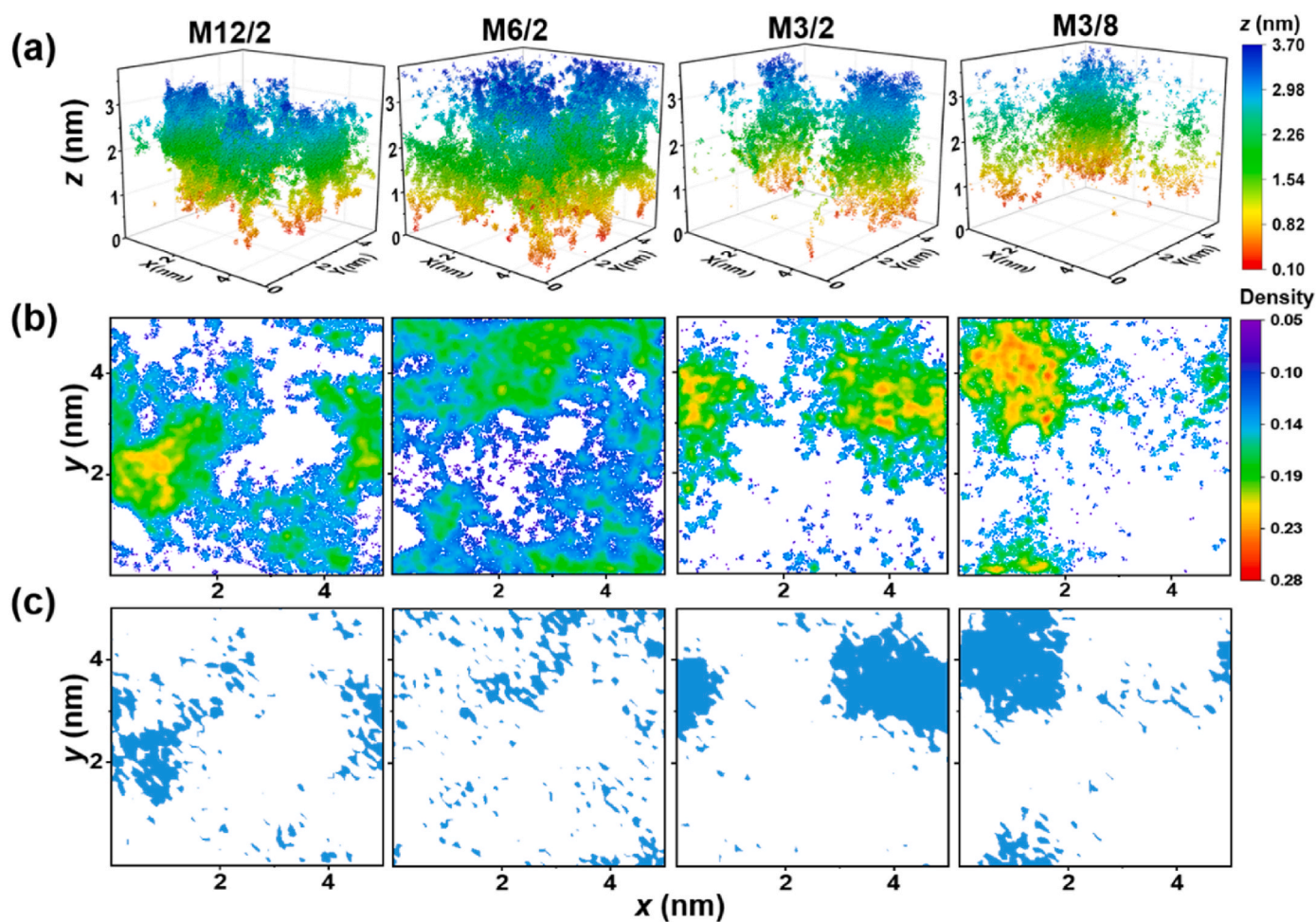


Fig. 5. Three-dimensional distribution of water molecules within the membrane (a) and their projected density map on the  $xy$ -plane (b). Permeation paths distribution on the  $xy$ -plane (c).

prefer to permeate from these regions, thereby minimizing the resistance caused by lateral movement within the membrane and enhancing the permeation efficiency. In contrast, the water distribution in the M12/2 membrane appears slightly more tortuous, while in the M6/2 membrane, water molecules are distributed almost throughout the entire membrane without distinct accumulation regions. This suggests that the transport pathways are more complex, requiring water molecules to continuously search for low-resistance regions to complete transmembrane permeation, thereby reducing the efficiency.

To better visualize the movement pathways of water molecules within the membranes, for each case, two water molecules are randomly selected from those whose residence time within the membrane is around the average residence time. Their trajectories are recorded in Fig. S2. The results are consistent with the above findings. In the high-permeance M3/2 and M3/8 membranes, water molecules pass through the membrane almost in a straight line with minimal lateral movement, demonstrating high transport efficiency. In contrast, in the lower-permeance M12/2 membrane, a lot of lateral movements are

observed in the trajectories, indicating that water molecules encounter greater resistance during transmembrane transport. For the M6/2 membrane, which exhibits the lowest permeance, the movement trajectories of the water molecules are the most complex, with notably tortuous paths, suggesting that the water molecules undergo multiple lateral movements within the M6/2 membrane.

To identify the regions where water molecules can permeate rapidly, we divide the *xy*-plane into a  $51 \times 51$  grid and calculate the cumulative *z*-axis displacement of water molecules within each grid cell. These displacement data are ranked, and a two-segment linear fitting method is applied to determine the distribution inflection point. Regions with cumulative displacements exceeding this threshold are defined as permeation paths (method in the supplementary materials).

As shown in Fig. 5(c), the identified permeation paths closely correspond to high-density water molecule regions, confirming their role as primary permeation pathways. The M12/2 and M6/2 membranes exhibit dispersed permeation paths, indicating discontinuous transport with complex pathways. In contrast, the M3/2 and M3/8 membranes have concentrated paths, suggesting lower transmembrane resistance and efficient water permeation.

This phenomenon is closely related to the density distribution characteristics of the membranes. The M12/2 and M6/2 membranes have a higher density, where the compact internal structure restricts the space available for permeation paths, resulting in a more dispersed transport pathway. In contrast, the M3/2 and M3/8 membranes have lower densities and greater structural flexibility. Under prolonged exposure to high-pressure water flow, their pore structures gradually expand, leading to the formation of concentrated and well-defined permeation paths regions.

Additionally, we calculate the total area of the water molecule distribution region and the permeation paths area. As shown in Fig. 6(a), in the M12/2 and M6/2 membranes, although the total water molecule distribution region is relatively large, the proportion of permeation paths is low. This indicates the presence of large inefficient transport regions, which is a key factor contributing to their lower overall water permeance. In contrast, the permeation path proportions in the M3/2 and M3/8 membranes are slightly higher than those in the M12/2 and M6/2 membranes, and their water molecule distribution regions are smaller. This indicates that these membranes contain more efficient transport pathways, which effectively reduce the lateral diffusion resistance and thereby increase the water permeability.

The structural characteristics of the permeation paths within the membranes have a significant impact on the transmembrane transport efficiency of both water molecules and salt ions. Furthermore, the structural differences in the permeation paths across different membrane systems determine the relative contributions of water molecules and salt ions to the total permeance. As shown in Fig. 6(b), the proportions of water molecules and ions within the permeation paths are

both relatively high, with water molecules accounting for over 70 % and salt ions over 80 %. This indicates that the majority of permeance contributions originate from the permeation paths. On the other hand, due to their larger hydrated diameters, salt ions exhibit a stronger dependence on the paths. In regions that are too narrow for water molecules to access, the possibility of ion permeation is extremely low.

### 3.4. Transport behaviors of ions through NF membranes

The exceptional separation performance of polyamide NF membranes for monovalent and divalent ions underpins their broad potential for industrial applications. Ion transport across the membrane is influenced not only by the intrinsic ion size but also by the dynamic evolution of its hydration shell. The hydration shell significantly increases the effective diameter of the ion, necessitating partial dehydration for passage through nanometer-scale membrane pores. Therefore, investigating the dehydration behavior of ions during transmembrane transport is crucial for elucidating the membrane separation mechanism. In this study, by comparing the dehydration behavior of  $\text{Na}^+$  and  $\text{Mg}^{2+}$  in different membrane systems, we clarify how different membrane structures regulate ion dehydration and thereby influence separation performance.

As shown in Fig. 7(a), when  $\text{Na}^+$  ions enter the membrane, their first hydration shell remains almost stable, with the coordination number decreasing by only 8 %–12 %. In contrast, the dehydration of the second hydration shell is much more pronounced (22 %–30 %), indicating that the dehydration of  $\text{Na}^+$  is attributable to the removal of the second hydration shell. Importantly,  $\text{Na}^+$  exhibits a higher degree of dehydration in both the first and second hydration shells in the M12/2 and M6/2 membranes than in M3/2 and M3/8 membranes, which can be attributed to the denser and more tortuous pore structures in the former two membranes.

For  $\text{Mg}^{2+}$ , due to the nearly 100 % rejection rate of the M12/2 and M6/2 membranes, effective permeation data can only be obtained from the M3/2 and M3/8 membranes. Since the first hydration shell of  $\text{Mg}^{2+}$  remains essentially intact during the permeation process, it is excluded from Fig. 7. In contrast, the degree of dehydration in the second hydration shell of  $\text{Mg}^{2+}$  is comparable to that of  $\text{Na}^+$ , suggesting that  $\text{Mg}^{2+}$  primarily relies on the removal of the second hydration shell to enable transmembrane transport.

Compared to  $\text{Na}^+$ ,  $\text{Mg}^{2+}$  has a higher valence state and a smaller ionic radius, which results in a higher charge density and stronger Coulomb interactions with surrounding water molecules [57,58]. As a consequence, its hydration shell remains more stable, particularly in the first hydration layer, which is nearly resistant to dehydration. These characteristics significantly increase the spatial exclusion and sieving effects encountered by  $\text{Mg}^{2+}$  during transmembrane transport. While the degree of dehydration in the second hydration shell of  $\text{Mg}^{2+}$  is

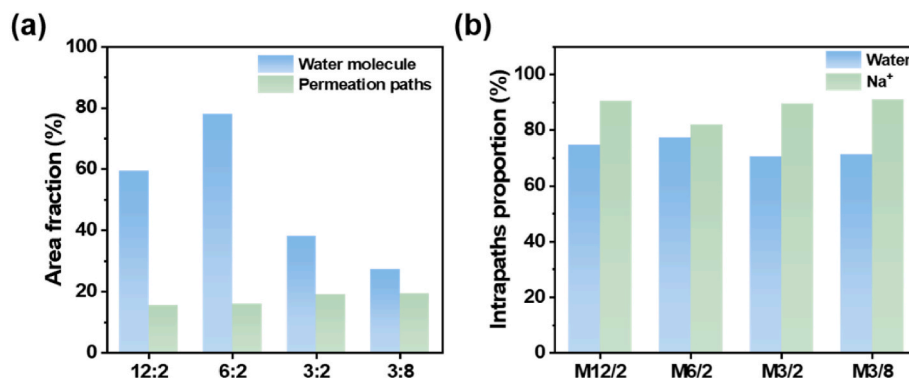


Fig. 6. (a) Area fractions of the water molecule distribution and the permeation paths distribution; (b) Proportions of water molecules and ions within the permeation paths.

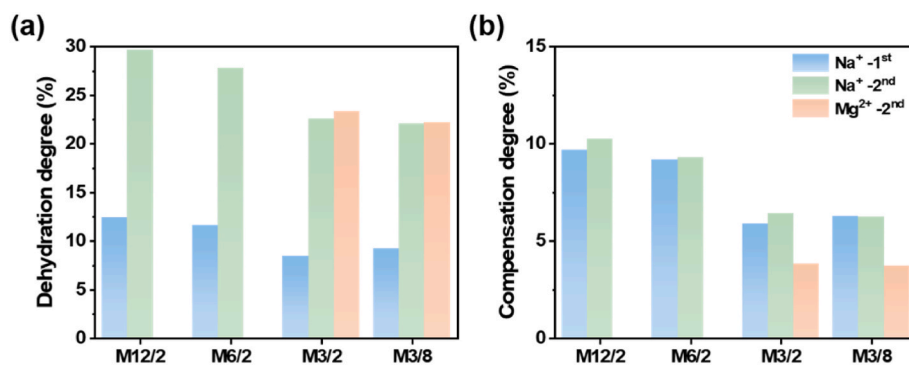


Fig. 7. Degree of ion dehydration (a) and hydration compensation (b) in membranes.

similar to that of Na<sup>+</sup>, its substantially higher hydration free energy and the persistent resistance of its intact first hydration shell continue to hinder its permeation through the membrane.

It has been discovered that the atoms on the pore walls can compensate for the ion hydration shell, partially offsetting the dehydration effect and reducing the free energy barrier that ions must overcome during membrane permeation [59–61]. As shown in Fig. 7(b), the compensation effect on the first hydration shell of Na<sup>+</sup> nearly restores its coordination number to the bulk phase level, whereas the compensation for the second hydration shell (including that of Mg<sup>2+</sup>) is significantly lower. This discrepancy is attributed to the significantly lower hydration free energy of the second shell compared to the first.

To quantify this phenomenon, we introduce the Hydration Recovery Ratio (HRR) as an indicator of the extent to which the PA membrane participates in ion hydration. HRR is defined as the ratio of hydration compensation to dehydration, expressed as:

$$\text{HRR} = \frac{D_{\text{compensation}}}{D_{\text{dehydration}}} \times 100\% \quad (3)$$

where  $C_{\text{compensation}}$  and  $D_{\text{dehydration}}$  represent the degrees of hydration compensation and dehydration, respectively. As shown in Table 2, the HRR values for M12/2 and M6/2 membranes are similar, but significantly larger than those of M3/2 and M3/8 membranes.

However, while a high HRR suggests that the pore structure effectively “restores” the ion hydration shell, it also indicates stronger interactions between the ions and the pore walls. This enhanced interaction increases the adhesive forces of ions within the pore walls, ultimately increasing the resistance to ion transport across the membranes [62]. This finding also explains why the ion rejection is higher in the M12/2 and M6/2 membranes.

During ion-transmembrane transport, the peak of the free energy barrier typically occurs at the point of minimum hydration degree. Herein, a statistical analysis is conducted on the minimum hydration number of each ion that successfully permeates the membrane under different conditions, aimed at elucidating the critical role of pore heterogeneity in modulating ion dehydration behavior.

As shown in Fig. 8(a), for the first hydration shell of Na<sup>+</sup>, most ions need to shed two water molecules to successfully traverse the membrane. In highly dense membranes (M12/2, M6/2), over 20 % of the ions have to reduce their hydration number to three, while in less dense

**Table 2**  
Hydration recovery ratio of ions within the membrane.

Case Name	HRR(%)		
	Na <sup>+</sup> -1 <sup>st</sup>	Na <sup>+</sup> -2 <sup>nd</sup>	Mg <sup>2+</sup> -2 <sup>nd</sup>
M12/2	77.97	34.60	/
M6/2	79.08	33.43	/
M3/2	70.03	28.41	16.45
M3/8	67.91	28.22	16.77

membranes (M3/2, M3/8), more than 25 % of the ions can permeate with only one water molecule removed. This indicates that highly dense membranes impose stricter dehydration requirements for ion transport.

Fig. 8(b) further examines the second hydration shell, revealing a similar trend that highly dense membranes require the removal of more outer shell water molecules for successful ion permeation. This combined dehydration constraint suggests that the narrowest bottlenecks in highly dense membranes compel ions to simultaneously strip both the first and second hydration shells, significantly increasing transmembrane resistance. In contrast, the looser structure of less dense membranes substantially reduces this resistance.

In summary, ion transport resistance is primarily governed by the degree of hydration compatibility at the narrowest pore regions. This finding provides direct insights into optimizing pore uniformity to balance membrane selectivity and permeability.

#### 4. Conclusion

In this work, MD simulations clarify the mechanism by which monomer concentrations regulate the structure and separation properties of polyamide nanofiltration membranes. It is demonstrated that monomer concentration not only directly governs the thickness and DNC of the PA membrane but also profoundly shapes its morphological characteristics by modulating the delicate kinetic interplay between the diffusion of the two monomers during interfacial polymerization. While a relatively higher PIP concentration tends to establish a broader potential reaction zone via deeper diffusion, the concentration and distribution of TMC ultimately dictate the effective utilization of this zone and the actual depth of reaction. Specifically, insufficient TMC in the deeper organic phase can cause diffused PIP to return towards the interface, resulting in a narrower reaction zone and a thinner membrane. Conversely, an appropriate TMC concentration that aligns with the PIP diffusion front promotes PIP reaction further into the organic phase, leading to membrane thickening. However, an excessively high TMC concentration, particularly if it establishes a steep concentration gradient at the interface, can lead to rapid formation of a dense interfacial layer, thereby restricting further PIP penetration and the expansion of the reaction zone, ultimately also resulting in a thinner membrane. Furthermore, regardless of the membrane thickness, an elevated PIP concentration tends to yield a more compact membrane structure.

Membranes with high cross-linking and density, which is formed in the molar ratio of PIP/TMC at 6/2, exhibit superior salt rejection, 65 % Na<sup>+</sup> and 94.2 % Mg<sup>2+</sup> rejection, at the cost of reduced water permeance, around 100 LMHB. Less dense structures, which is formed in the case of M3/8, offer higher flux but lower ion rejection. Ion dehydration and the compensatory role of pore-wall interactions are shown to be key factors in modulating ion transport resistance. Overall, achieving a proper balance of monomer concentrations can realize membranes with optimized structure and efficient separation performance. These insights

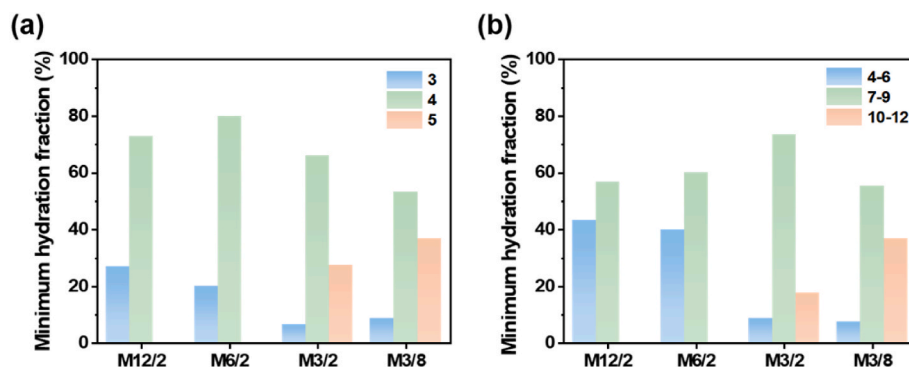


Fig. 8. Minimum number of water molecules in the first (a) and the second (b) hydration shells of  $\text{Na}^+$ .

provide valuable theoretical support for the design and optimization of advanced nanofiltration membranes.

Furthermore, future research should also address the exothermic effects of interfacial polymerization, a factor commonly overlooked in current simulation studies. These thermal effects are complex and not yet fully understood, but they are increasingly recognized as a significant factor influencing polyamide membrane morphology [63,64]. Developing simulation methods capable of capturing polymerization exothermicity, coupled with expanding simulation scales as computational capabilities advance, will be crucial for a deeper understanding of the interfacial polymerization process.

#### CRediT authorship contribution statement

**Gan Liu:** Writing – original draft, Investigation, Data curation. **Mingjie Wei:** Writing – review & editing, Validation, Funding acquisition. **Zhaoqin Xu:** Methodology, Investigation. **Daiwen Li:** Investigation. **Ming Liu:** Investigation. **Jun Huang:** Validation, Methodology. **Zhe Zhang:** Validation, Methodology. **Yong Wang:** Writing – review & editing, Supervision, Funding acquisition, Conceptualization.

#### Declaration of generative AI and AI-assisted technologies in the writing process

During the preparation of this work the authors used ChatGPT-4.0 in order to improve the readability and language of the manuscript. After using this tool, the authors reviewed and edited the content as needed and take full responsibility for the content of the published article.

#### Declaration of competing interest

The authors declare that they have no known competing financial interests or personal relationships that could have appeared to influence the work reported in this paper.

#### Acknowledgement

This work was financially supported by the National Natural Science Foundation of China (22278206, 22308147). The authors also thank the High Performance Computing Centre of Nanjing Tech University for supporting the computational resources.

#### Appendix A. Supplementary data

Supplementary data to this article can be found online at <https://doi.org/10.1016/j.memsci.2025.124334>.

#### Data availability

Data will be made available on request.

#### References

- [1] J.R. Werber, C.O. Osuji, M. Elimelech, Materials for next-generation desalination and water purification membranes, *Nat. Rev. Mater.* 1 (5) (2016), <https://doi.org/10.1038/natrevmats.2016.18>.
- [2] J.R. Werber, A. Deshmukh, M. Elimelech, The critical need for increased selectivity, not increased water permeability, for desalination membranes, *Environ. Sci. Technol. Lett.* 3 (4) (2016) 112–120, <https://doi.org/10.1021/acs.estlett.6b00050>.
- [3] A.W. Mohammad, Y.H. Teow, W.L. Ang, Y.T. Chung, D.L. Oatley-Radcliffe, N. Hilal, Nanofiltration membranes review: recent advances and future prospects, *Desalination* 356 (2015) 226–254, <https://doi.org/10.1016/j.desal.2014.10.043>.
- [4] H.Y. Peng, S.K. Lau, W.F. Yong, Recent advances of thin film composite nanofiltration membranes for  $\text{Mg}^{2+}/\text{Li}^+$  separation, *Advanced Membranes* 4 (2024), <https://doi.org/10.1016/j.advmem.2024.100093>.
- [5] D. Lu, Z. Yao, L. Jiao, M. Waheed, Z. Sun, L. Zhang, Separation mechanism, selectivity enhancement strategies and advanced materials for mono-/multivalent ion-selective nanofiltration membrane, *Advanced Membranes* 2 (2022), <https://doi.org/10.1016/j.advmem.2022.100032>.
- [6] L.E. Peng, Z.K. Yao, Z. Yang, H. Guo, C.Y. Tang, Dissecting the role of substrate on the morphology and separation properties of thin film composite polyamide membranes: seeing is believing, *Environ. Sci. Technol.* 54 (11) (2020) 6978–6986, <https://doi.org/10.1021/acs.est.0c01427>.
- [7] J.T. Wang, R.Z. Xu, F. Yang, J. Kang, Y. Cao, M. Xiang, Probing influences of support layer on the morphology of polyamide selective layer of thin film composite membrane, *J. Membr. Sci.* 556 (2018) 374–383, <https://doi.org/10.1016/j.memsci.2018.04.011>.
- [8] X. Li, K.Y. Wang, B. Helmer, T.S. Chung, Thin-film composite membranes and formation mechanism of thin-film layers on hydrophilic cellulose acetate propionate substrates for forward osmosis processes, *Ind. Eng. Chem. Res.* 51 (30) (2012) 10039–10050, <https://doi.org/10.1021/ie2027052>.
- [9] M.F. Jimenez-Solomon, P. Gorgojo, M. Munoz-Ibanez, A.G. Livingston, Beneath the surface: influence of supports on thin film composite membranes by interfacial polymerization for organic solvent nanofiltration, *J. Membr. Sci.* 448 (2013) 102–113, <https://doi.org/10.1016/j.memsci.2013.06.030>.
- [10] L.W. Huang, J.R. McCutcheon, Impact of support layer pore size on performance of thin film composite membranes for forward osmosis, *J. Membr. Sci.* 483 (2015) 25–33, <https://doi.org/10.1016/j.memsci.2015.01.025>.
- [11] A.K. Ghosh, E.M.V. Hoek, Impacts of support membrane structure and chemistry on polyamide-polysulfone interfacial composite membranes, *J. Membr. Sci.* 336 (1–2) (2009) 140–148, <https://doi.org/10.1016/j.memsci.2009.03.024>.
- [12] Z. Yang, F. Wang, H. Guo, L.E. Peng, X.H. Ma, X.X. Song, Z.W. Wang, C.Y. Tang, Mechanistic insights into the role of polydopamine interlayer toward improved separation performance of polyamide nanofiltration membranes, *Environ. Sci. Technol.* 54 (18) (2020) 11611–11621, <https://doi.org/10.1021/acs.est.0c03589>.
- [13] G.Z. Ramon, M.C.Y. Wong, E.M.V. Hoek, Transport through composite membrane, part 1: is there an optimal support membrane? *J. Membr. Sci.* 415 (2012) 298–305, <https://doi.org/10.1016/j.memsci.2012.05.013>.
- [14] J.G. Wijmans, P.J. Hao, Influence of the porous support on diffusion in composite membranes, *J. Membr. Sci.* 494 (2015) 78–85, <https://doi.org/10.1016/j.memsci.2015.07.047>.
- [15] S. Mondal, I.M. Griffiths, G.Z. Ramon, Frontiers in structure-performance models of separation membranes, *J. Membr. Sci.* 588 (2019), <https://doi.org/10.1016/j.memsci.2019.06.006>.
- [16] R.J. Petersen, Composite reverse-osmosis and nanofiltration membranes, *J. Membr. Sci.* 83 (1) (1993) 81–150, [https://doi.org/10.1016/0376-7388\(93\)80014-0](https://doi.org/10.1016/0376-7388(93)80014-0).
- [17] C.Y.Y. Tang, Y.N. Kwon, J.O. Leckie, Effect of membrane chemistry and coating layer on physicochemical properties of thin film composite polyamide RO and NF membranes I. FTIR and XPS characterization of polyamide and coating layer chemistry, *Desalination* 242 (1–3) (2009) 149–167, <https://doi.org/10.1016/j.desal.2008.04.003>.
- [18] J. Wei, X.G. Jian, C.R. Wu, S.H. Zhang, C. Yan, Influence of polymer structure on thermal stability of composite membranes, *J. Membr. Sci.* 256 (1–2) (2005) 116–121, <https://doi.org/10.1016/j.memsci.2005.02.012>.

- [19] A.P. Rao, S.V. Joshi, J.J. Trivedi, C.V. Devmurari, V.J. Shah, Structure-performance correlation of polyamide thin film composite membranes: effect of coating conditions on film formation, *J. Membr. Sci.* 211 (1) (2003) 13–24, [https://doi.org/10.1016/S0376-7388\(02\)00305-8](https://doi.org/10.1016/S0376-7388(02)00305-8).
- [20] A.E. Childress, M. Elimelech, Relating nanofiltration membrane performance to membrane charge (electrokinetic) characteristics, *Environ. Sci. Technol.* 34 (17) (2000) 3710–3716, <https://doi.org/10.1021/es0008620>.
- [21] K. Kosutic, L. Kastelan-Kunst, B. Kunst, Porosity of some commercial reverse osmosis and nanofiltration polyamide thin-film composite membranes, *J. Membr. Sci.* 168 (1–2) (2000) 101–108, [https://doi.org/10.1016/S0376-7388\(99\)00309-9](https://doi.org/10.1016/S0376-7388(99)00309-9).
- [22] B. Mi, O. Coronell, B. Marinas, F. Watanabe, D. Cahill, I. Petrov, Physico-chemical characterization of NF/RO membrane active layers by rutherford backscattering spectrometry, *J. Membr. Sci.* 282 (1–2) (2006) 71–81, <https://doi.org/10.1016/j.memsci.2006.05.015>.
- [23] B. Van der Bruggen, J.C. Jansen, A. Figoli, J. Geens, D. Van Baelen, E. Drioli, C. Vandecasteele, Determination of parameters affecting transport in polymeric membranes: parallels between pervaporation and nanofiltration, *J. Phys. Chem. B* 108 (35) (2004) 13273–13279, <https://doi.org/10.1021/jp048249g>.
- [24] N.K. Saha, S.V. Joshi, Performance evaluation of thin film composite polyamide nanofiltration membrane with variation in monomer type, *J. Membr. Sci.* 342 (1–2) (2009) 60–69, <https://doi.org/10.1016/j.memsci.2009.06.025>.
- [25] A.K. Ghosh, B.H. Jeong, X.F. Huang, E.M.V. Hoek, Impacts of reaction and curing conditions on polyamide composite reverse osmosis membrane properties, *J. Membr. Sci.* 311 (1–2) (2008) 34–45, <https://doi.org/10.1016/j.memsci.2007.11.038>.
- [26] Y.Q. Zhang, H. Wang, J. Guo, X.Q. Cheng, G. Han, C.H. Lau, H.Q. Lin, S.M. Liu, J. Ma, L. Shao, Ice-confined synthesis of highly ionized 3D-quasilayered polyamide nanofiltration membranes, *Science* 382 (6667) (2023) 202–206, <https://doi.org/10.1126/science.ad9531>.
- [27] S. Karan, Z. Jiang, A.G. Livingston, Sub-10 nm polyamide nanofilms with ultrafast solvent transport for molecular separation, *Science* 348 (6241) (2015) 1347–1351, <https://doi.org/10.1126/science.aaa5058>.
- [28] Q.-W. Meng, L. Cheng, Q. Ge, Recent advances and future challenges of polyamide-based chlorine-resistant membrane, *Advanced Membranes* 3 (2023) 100075, <https://doi.org/10.1016/j.advmem.2023.100075>.
- [29] Z. Wang, X. Luo, J. Zhang, F. Zhang, W. Fang, J. Jin, Polymer membranes for organic solvent nanofiltration: recent progress, challenges and perspectives, *Advanced Membranes* 3 (2023) 100063, <https://doi.org/10.1016/j.advmem.2023.100063>.
- [30] R.Y. Wang, S.H. Lin, Pore model for nanofiltration: history, theoretical framework, key predictions, limitations, and prospects, *J. Membr. Sci.* 620 (2021), <https://doi.org/10.1016/j.memsci.2020.118809>.
- [31] M.R. Chowdhury, J. Steffes, B.D. Huey, J.R. McCutcheon, 3D printed polyamide membranes for desalination, *Science* 361 (6403) (2018) 682–685, <https://doi.org/10.1126/science.aar2122>.
- [32] Z. Tan, S.F. Chen, X.S. Peng, L. Zhang, C.J. Gao, Polyamide membranes with nanoscale turing structures for water purification, *Science* 360 (6388) (2018) 518, <https://doi.org/10.1126/science.aar6308>.
- [33] J.E. Gu, S. Lee, C.M. Stafford, J.S. Lee, W. Choi, B.Y. Kim, K.Y. Baek, E.P. Chan, J. Y. Chung, J. Bang, J.H. Lee, Molecular layer-by-layer assembled thin-film composite membranes for water desalination, *Adv. Mater.* 25 (34) (2013) 4778–4782, <https://doi.org/10.1002/adma.201302030>.
- [34] T.E. Culp, B. Khara, K.P. Brickey, M. Geitner, T.J. Zimudzi, J.D. Wilbur, S.D. Jons, A. Roy, M. Paul, B. Ganapathysubramanian, A.L. Zydney, M. Kumar, E.D. Gomez, Nanoscale control of internal inhomogeneity enhances water transport in desalination membranes, *Science* 371 (6524) (2021) 72–75, <https://doi.org/10.1126/science.abb8518>.
- [35] L. Shen, R.H. Cheng, M. Yi, W.S. Hung, S. Japip, L. Tian, X. Zhang, S.D. Jiang, S. Li, Y. Wang, Polyamide-based membranes with structural homogeneity for ultrafast molecular sieving, *Nat. Commun.* 13 (1) (2022), <https://doi.org/10.1038/s41467-022-28183-1>.
- [36] Q. Xue, W.Q. Meng, Y. Li, Q. Fang, K.S. Zhang, Tailored design of polyamide nanofiltration membrane with small-sized MXene quantum dots for promoting water transport, *J. Membr. Sci.* 699 (2024), <https://doi.org/10.1016/j.memsci.2024.122656>.
- [37] F. Soyekwo, H. Wen, D. Liao, C.K. Liu, Fouling-resistant ionic graft-polyamide nanofiltration membrane with improved permeance for lithium separation from MgCl/LiCl mixtures, *J. Membr. Sci.* 659 (2022), <https://doi.org/10.1016/j.memsci.2022.120773>.
- [38] C. Jiang, Z.Y. Liu, L. Jiang, Z.H. Fei, Y.F. Hou, Rapid transport of water and monovalent ions through ultrathin polyamide nanofilms for highly efficient mono/bivalent ions separation, *Appl. Surf. Sci.* 608 (2023), <https://doi.org/10.1016/j.apsusc.2022.155025>.
- [39] S.W. Liu, S. Ganti-Agrawal, S. Keten, R.M. Lueptow, Molecular insights into charged nanofiltration membranes: structure, water transport, and water diffusion, *J. Membr. Sci.* 644 (2022), <https://doi.org/10.1016/j.memsci.2021.120057>.
- [40] A.I. Jewett, D. Stelter, J. Lambert, S.M. Saladi, O.M. Roscioni, M. Ricci, L. Autin, M. Maritan, S.M. Bashusqeh, T. Keyes, R.T. Dame, J.E. Shea, G.J. Jensen, D. S. Goodsell, Moltemplate: a tool for coarse-grained modeling of complex biological matter and soft condensed matter physics, *J. Mol. Biol.* 433 (11) (2021), <https://doi.org/10.1016/j.jmb.2021.166841>.
- [41] W. Zhang, R. Chu, W. Shi, Y. Hu, Quantitatively unveiling the activity-structure relationship of polyamide membrane: a molecular dynamics simulation study, *Desalination* 528 (2022), <https://doi.org/10.1016/j.desal.2022.115640>.
- [42] H. Zhang, M.S. Wu, K. Zhou, A.W.K. Law, Molecular insights into the composition-structure-property relationships of polyamide thin films for reverse osmosis desalination, *Environ. Sci. Technol.* 53 (11) (2019) 6374–6382, <https://doi.org/10.1021/acs.est.9b02214>.
- [43] Y. Liu, J.F. Kong, X.Y. Bian, Y.P. Zhang, M.Z. Ji, Q. Peng, J. Jin, Y.Z. Zhu, Positively charged Poly(Piperazinamide) nanofiltration membranes for the fast removal of metal ions, *Adv. Mater. Interfac.* 9 (33) (2022), <https://doi.org/10.1002/admi.202201206>.
- [44] G. Liu, M.J. Wei, D.W. Li, M. Liu, J. Huang, Y. Wang, Understanding interfacial polymerization in the formation of polyamide RO membranes by molecular simulations, *Desalination* 586 (2024), <https://doi.org/10.1016/j.desal.2024.117869>.
- [45] L.J. Abbott, K.E. Hart, C.M. Colina, Polymatic: a generalized simulated polymerization algorithm for amorphous polymers, *Theor. Chem. Acc.* 132 (3) (2013) 1334, <https://doi.org/10.1007/s00214-013-1334-z>.
- [46] C. Jang, T.W. Sirk, J.W. Andzelm, C.F. Abrams, Comparison of crosslinking algorithms in molecular dynamics simulation of thermosetting polymers, *Macromol. Theory Simul.* 24 (3) (2015) 260–270, <https://doi.org/10.1002/mats.201400094>.
- [47] X. Zhang, M.J. Wei, F. Xu, Y. Wang, Thickness-dependent ion rejection in nanopores, *J. Membr. Sci.* 601 (2020), <https://doi.org/10.1016/j.memsci.2020.117899>.
- [48] S. Plimpton, Fast parallel algorithms for short-range molecular-dynamics, *J. Comput. Phys.* 117 (1) (1995) 1–19, <https://doi.org/10.1006/jcph.1995.1039>.
- [49] J. Jang, R.M. Wolf, J.W. Caldwell, P.A. Kollman, D.A. Case, Development and testing of a general amber force field, *J. Comput. Chem.* 25 (9) (2004) 1157–1174, <https://doi.org/10.1002/jcc.20035>.
- [50] S.P. Kadaoluwa Pathirannahalage, N. Meftahi, A. Elbourne, A.C.G. Weiss, C. F. McConville, A. Padua, D.A. Winkler, M. Costa Gomes, T.L. Greaves, T.C. Le, Q. A. Besford, A.J. Christofferson, Systematic comparison of the structural and dynamic properties of commonly used water models for molecular dynamics simulations, *J. Chem. Inf. Model.* 61 (9) (2021) 4521–4536, <https://doi.org/10.1021/acs.jcim.1c00794>.
- [51] M. Shen, S. Keten, R.M. Lueptow, Rejection mechanisms for contaminants in polyamide reverse osmosis membranes, *J. Membr. Sci.* 509 (2016) 36–47, <https://doi.org/10.1016/j.memsci.2016.02.043>.
- [52] M.Q. Seah, W.J. Lau, P.S. Goh, H.H. Tseng, R.A. Wahab, A.F. Ismail, Progress of interfacial polymerization techniques for polyamide thin film (nano)Composite membrane fabrication: a comprehensive review, *Polymers* 12 (12) (2020), <https://doi.org/10.3390/polym12122817>.
- [53] Z.W. Jiang, S. Karan, A.G. Livingston, Water transport through ultrathin polyamide nanofilms used for reverse osmosis, *Adv. Mater.* 30 (15) (2018), <https://doi.org/10.1002/adma.201705973>.
- [54] Y. Song, M.J. Wei, F. Xu, Y. Wang, Transport mechanism of water molecules passing through polyamide/COF mixed matrix membranes, *Phys. Chem. Chem. Phys.* 21 (48) (2019) 26591–26597, <https://doi.org/10.1039/c9cp05026d>.
- [55] V. Freger, S. Srebnik, Mathematical model of charge and density distributions in interfacial polymerization of thin films, *J. Appl. Polym. Sci.* 88 (5) (2003) 1162–1169, <https://doi.org/10.1002/app.11716>.
- [56] S.Z. Zheng, J. Gissing, B.S. Hsiao, T. Wei, Interfacial polymerization of aromatic polyamide reverse osmosis membranes, *ACS Appl. Mater. Interfaces* 16 (47) (2024) 65677–65686, <https://doi.org/10.1021/acsami.4c16229>.
- [57] Y. Yuan, W.Q. Zhan, H. Yi, Y.L. Zhao, S.X. Song, Molecular dynamics simulations study for the effect of cations hydration on the surface tension of the electrolyte solutions, *Colloids Surf. A Physicochem. Eng. Asp.* 539 (2018) 80–84, <https://doi.org/10.1016/j.colsurfa.2017.12.005>.
- [58] B. Tansel, Significance of thermodynamic and physical characteristics on permeation of ions during membrane separation: hydrated radius, hydration free energy and viscous effects, *Sep. Purif. Technol.* 86 (2012) 119–126, <https://doi.org/10.1016/j.seppur.2011.10.033>.
- [59] D. Cohen-Tanugi, J.C. Grossman, Water desalination across nanoporous graphene, *Nano Lett.* 12 (7) (2012) 3602–3608, <https://doi.org/10.1021/nl3012853>.
- [60] Y. Kang, Z.S. Zhang, H. Shi, J.Q. Zhang, L.J. Liang, Q. Wang, H. Agren, Y.Q. Tu, Na and K ion selectivity by size-controlled biomimetic graphene nanopores, *Nanoscale* 6 (18) (2014) 10666–10672, <https://doi.org/10.1039/c4nr01383b>.
- [61] Y.J. Chen, Y.D. Zhu, Y. Ruan, N.N. Zhao, W. Liu, W. Zhuang, X.H. Lu, Molecular insights into multilayer 18-crown-6-like graphene nanopores for K/Na separation: a molecular dynamics study, *Carbon* 144 (2019) 32–42, <https://doi.org/10.1016/j.carbon.2018.11.048>.
- [62] F. Xu, M.J. Wei, Y. Wang, Effect of hydrophilicity on ion rejection of sub-nanometer pores, *Sep. Purif. Technol.* 257 (2021), <https://doi.org/10.1016/j.seppur.2020.117937>.
- [63] V. Freger, Nanoscale heterogeneity of polyamide membranes formed by interfacial polymerization, *Langmuir* 19 (11) (2003) 4791–4797, <https://doi.org/10.1021/la020920q>.
- [64] A. Deshmukh, J.H. Lienhard, M. Elimelech, Heat diffusion during thin-film composite membrane formation, *J. Membr. Sci.* 696 (2024), <https://doi.org/10.1016/j.memsci.2024.122493>.